Available online at www.sciencedirect.com

ScienceDirect

Procedia Structural Integrity 68 (2025) 1294–1300

Structural Integrity Procedia

www.elsevier.com/locate/procedia

European Conference on Fracture 2024 (ECF24)

Experiments and numerical simulations on low cycle ductile damage and failure under shear loading conditions

Steffen Gerke[a,*], Zhichao Wei[a,b], Marleen Harting[a], Michael Brünig[a]

[a]*Institut für Mechanik und Statik, Universität der Bundeswehr München, Werner-Heisenberg-Weg 39, D-85577 Neubiberg, Germany*
[b]*Institut für Bildsame Formgebung, RWTH Aachen University, Intzestr. 10, D-52072 Aachen, Germany*

Abstract

Ductile damage is an irreversible process that may appear during the service life of engineering structures, resulting in the degradation of material elastic behavior. Its accumulation ultimately leads to failure. An advanced phenomenological cyclic plastic-damage continuum model is employed to predict material behavior under reverse loading conditions. The Bauschinger effect, stress differential effect, and non-hardening effects are taken into account to more accurately capture plastic and damage deformations. In this context reverse cyclic shear loading is of special interest and corresponding experiments can be conducted with specially designed specimens on a standard testing device. For this loading scenario stress triaxialities remain nearly constant with values of approximately 0 during load reversal. Moreover, this shear loading sequence influences the material behavior at both macro- and micro-levels. Thus, a series of novel reverse cyclic shear experiments is realized to analyze this influence in detail. The digital image correlation technique records the deformations and changes in strains during the experiments, and selected fracture surfaces are examined by scanning electron microscopy to verify the damage and fracture mechanisms. The numerical results regarding load-displacement curves and strain fields are compared with the experimental ones.

Keywords: Ductile damage and failure; Low cycle reverse shear experiments;

1. Introduction

Ductile damage has been widely discussed in recent decades, as it degrades the material's elastic properties and reduces its bearing capability. Therefore, accurately predicting the occurrence and evolution of ductile damage in various engineering applications is essential to characterize failure behavior and avoiding engineering accidents. In contrast, fatigue damage is another important phenomenon, resulting from strain localization under cyclic loading with a high number of cycles and relatively small plastic strains whereas ductile damage is accompanied by large plastic deformations, see for instance Murakami and Miller (2005); Kanvinde and Deierlein (2007); Cao et al. (2009);

* Corresponding author. Tel.: +49-89-6004-3422.
E-mail address: steffen.gerke@unibw.de

2452-3216
10.1016/j.prostr.2025.06.201

Shi et al. (2011); Daroju et al. (2022). Various uniaxial tension-compression cyclic experiments have been performed to study the influence of reverse loading on the occurrence and evolution of ductile damage and fracture behavior (Voyiadjis et al., 2013; Marcadet and Mohr, 2015; Klingbeil et al., 2016; Daroju et al., 2022; Wei et al., 2022; Wu et al., 2024). In addition, Algarni et al. (2019) performed a series of uniaxial tension-compression cyclic experiments with cylindrical specimens, using various loading cycles (e.g., 10, 21, 41, 51 cycles) to study damage accumulation and ductile fracture behavior. Wei et al. (2022) also pointed out that the loading sequence and the number of loading cycles also affect material behavior, based on experimental and numerical analyses of uniaxial tension-compression tests. Furthermore, this work considered the design of a new one-axis loaded shear specimen that minimizes significant rotation under cyclic loading. To extend previous work, novel shear cyclic loading tests with varying constant or increased amplitudes within large plastic deformations are designed. The digital image correlation technique is used to analyze the experimental results more accurately, and scanning electron microscopy is employed to investigate the ductile damage mechanisms.

The corresponding numerical simulations are based on an anisotropic cyclic plastic-damage model, considering the hardening changes after shear reverse loading and the Bauschinger effect. The constitutive model and numerical integration method are discussed by Wei et al. (2023, 2024) in detail, and the corresponding material parameters are also given in these publications. In this paper, the proposed material model is summarized in Section 2. Section 3 describes the experimental and numerical setups. The corresponding results are presented in Section 4, and finally, conclusions are provided in Section 5.

2. Material modeling

A hydrostatic–stress–dependent yield condition, incorporating combined hardening law, is used to characterize the onset of the yielding

$$f^{\mathrm{pl}} = \sqrt{\frac{1}{2}\,\mathrm{dev}(\bar{\mathbf{T}}-\bar{\boldsymbol{\alpha}})\cdot\mathrm{dev}(\bar{\mathbf{T}}-\bar{\boldsymbol{\alpha}})} - \bar{c}\left(1-\frac{a}{\bar{c}}\,\mathrm{tr}(\bar{\mathbf{T}}-\bar{\boldsymbol{\alpha}})\right) = \sqrt{\bar{J}_2} - \bar{c}(1-\frac{a}{\bar{c}}\bar{I}_1) = 0\,, \tag{1}$$

where $\bar{\mathbf{T}}$ represents the effective Kirchhoff stress tensor, $\bar{\boldsymbol{\alpha}}$ denotes the effective back stress tensor, $\bar{c}$ describes the current equivalent stress, $\frac{a}{\bar{c}}$ is the hydrostatic factor, and $\bar{I}_1$ and $\bar{J}_2$ are the first and second deviatoric effective reduced stress invariants, respectively. The combined hardening law is an additive combination of an isotropic hardening part ($\bar{c}$) and a kinematic hardening part ($\bar{\boldsymbol{\alpha}}$). In addition, it is assumed that the plastic deformations are isochoric. Consequently, the plastic potential function $g^{\mathrm{pl}}(\sqrt{\bar{J}_2})$ omits the influence of the hydrostatic stress term $\frac{a}{\bar{c}}\bar{I}_1$, and thus, the plastic strain rate tensor is defined as

$$\dot{\bar{\mathbf{H}}}^{\mathrm{pl}} = \dot{\lambda}\frac{\partial g^{\mathrm{pl}}(\sqrt{\bar{J}_2})}{\partial(\bar{\mathbf{T}}-\bar{\boldsymbol{\alpha}})} = \dot{\lambda}\frac{1}{2\sqrt{\bar{J}_2}}\,\mathrm{dev}(\bar{\mathbf{T}}-\bar{\boldsymbol{\alpha}}) = \dot{\gamma}\bar{\mathbf{N}}\,, \tag{2}$$

where $\dot{\lambda}$ is a non-negative multiplier, $\dot{\gamma}$ denotes the equivalent plastic strain increment, and $\bar{\mathbf{N}}$ represents the normalized deviatoric reduced stress tensor and defines the plastic strain increment direction.

Furthermore, the onset of damage is captured by the stress-state-dependent damage condition

$$f^{\mathrm{da}} = \hat{\alpha}\,\mathrm{tr}(\mathbf{T}-\boldsymbol{\alpha}) + \hat{\beta}\sqrt{\frac{1}{2}\,\mathrm{dev}(\mathbf{T}-\boldsymbol{\alpha})\cdot\mathrm{dev}(\mathbf{T}-\boldsymbol{\alpha})} - \tilde{\sigma} = \hat{\alpha}I_1 + \hat{\beta}\sqrt{J_2} - \tilde{\sigma} = 0\,, \tag{3}$$

where $\mathbf{T}$ is Kirchhoff stress tensor, $\boldsymbol{\alpha}$ denotes the damage back stress tensor, and I_1 and J_2 are the first and second deviatoric reduced stress invariants, respectively. The coefficients $\hat{\alpha}$ and $\hat{\beta}$ are stress-state-dependent, accounting for

different loading cases. As Brünig et al. (2008) pointed out, ductile damage mechanisms depend on different stress triaxialities. Damage caused by the growth of voids is governed by the volumetric part of the damage strain rate tensor $\dot{\mathbf{H}}^{\mathrm{da}}$, whereas damage resulting from micro-shear cracks is governed by the deviatoric part of $\dot{\mathbf{H}}^{\mathrm{da}}$. Thus, $\dot{\mathbf{H}}^{\mathrm{da}}$ is given by

$$\dot{\mathbf{H}}^{\mathrm{da}} = \dot{\mu}(\tilde{\alpha}\frac{1}{\sqrt{3}}\mathbf{1} + \tilde{\beta}\tilde{\mathbf{N}})\,, \tag{4}$$

where $\dot{\mu}$ is the rate equivalent damage strain, $\tilde{\mathbf{N}}$ describes the nominal transformed deviatoric reduced stress tensor, and $\tilde{\alpha}$ and $\tilde{\beta}$ are stress-state-dependent coefficients. More details on the material modeling can be found in Wei et al. (2023).

3. Experimental and numerical setup

To conduct experiments under reverse cyclic shear loading the symmetrical, double shear specimen presented in Wei et al. (2022), see Fig. 1(a), has been employed. The symmetrical arrangement of two shear zones avoids rotations of the clamped parts of the specimen and the material reduction in thickness direction of the shear zones ensures that high stress and strain concentrations occur only in these areas, resulting in here developing ductile damage. The notches have a depth of 1.0 mm on each side reducing the sheet thickness of 4.0 mm to the remaining minimum of 2.0 mm (Fig. 1(b)). Furthermore, the minimum notch length is 6.0 mm resulting in a cross section of 12.0 mm^2 on each side, see Fig. 1(c). The notches are aligned parallel to the loading direction which allows reverse cyclic shear loading without significant changes in stress triaxiality and Lode parameter. All specimens have been fabricated of high-strength aluminum–magnesium–silicon alloy EN-AW 6082-T6, see Wei et al. (2023) for details.

The in Section 2 presented constitutive model has been implemented via a user-defined subroutine in Ansys 18. The corresponding meshing has been realized with Ansys Solid185 hexahedral elements. As indicated in Fig. 1(d) remarkable mesh refinement in thickness direction in the notched region has been realized resulting in a minimum element edge length of 0.15 mm whereas the total number of elements has been 15,037. Furthermore, the simulations have been realized displacement controlled. All simulations, as well as those in previous publications, were carried out with the same set of material parameters, see Wei et al. (2023).

The experiments have been conducted on the standard electromechanical testing machine Inspekt Table 50-1 provided by Hegewald & Peschke, Germany. To ensure quasi-static loading conditions a constant machine velocity of 0.05 $\mathrm{mm/min}$ has been chosen for each load step. The displacements and strains of the specimen surfaces have been analyzed by a digital image correlation (DIC) system provided by Dantec/Limess while the machine force signal has been transmitted to the DIC system and the corresponding values have been stored with the DIC data sets. The DIC setup consists of two 6 MPx cameras equipped with 75 mm lenses while the evaluation has been realized with the related Istra4D software. The average camera resolution at the center of the specimen has been approximately 56 $\mathrm{Px/mm}$, and the subset (facet) size was selected to 33 Px with a grid spacing (overlap) of 11 Px while data sets have been saved with a frequency of 1 Hz. The relative displacement $\Delta u_{\mathrm{ref}} = u_{\mathrm{top}} - u_{\mathrm{bottom}}$ in loading direction of the two measuring points (red dots in Fig. 1(a)) has been chosen as appropriate displacement measure whereas for the numerical simulations the displacements of corresponding nodes have been evaluated in the same way. After the experiments, the fracture surfaces have been analyzed by scanning electron microscopy (SEM) with a Zeiss EVO 15.

4. Results

Fig. 2 displays the experimentally obtained as well as the numerically calculated load-displacement curves of the four different load cases where the fracture point of each experiment has been marked by solid black circle. For the curves displayed in Fig. 2(a, b) a maximum and minimum relative displacement has been determined prior to testing and cyclic loading has been applied until failure of the specimen. As the displacements of the testing machine have to be controlled, there are small differences in the minimum and maximum relative displacements. For the load

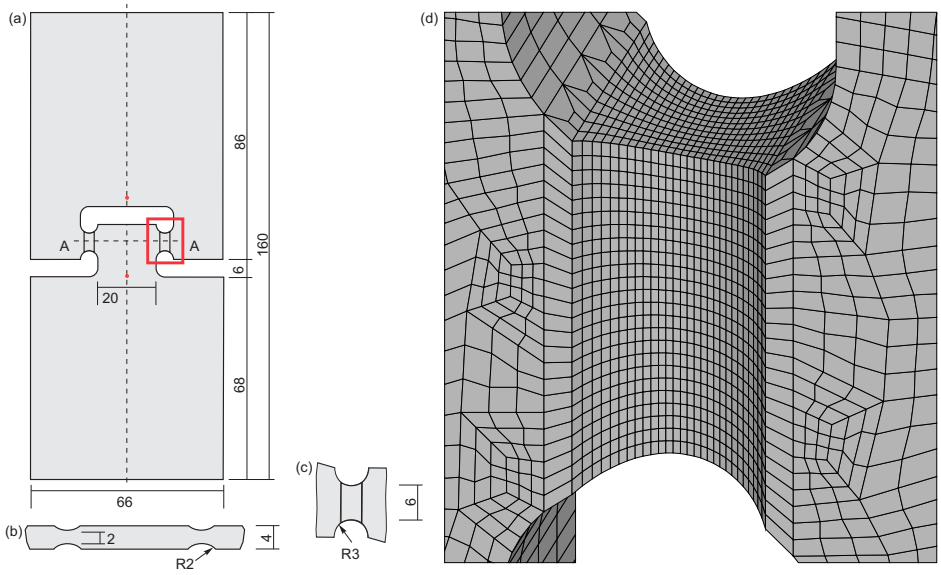

Fig. 1: (a) Specimen geometry; (b) cross section; (c) detail of notched part and (d) mesh of notched part, all measures in [mm].

case presented in (a) a maximum relative displacement of $\Delta u_{\text{ref}}^{\text{max}} = 0.5\,\text{mm}$ and a minimum relative displacement of $\Delta u_{\text{ref}}^{\text{min}} = -0.5\,\text{mm}$ are reported resulting in failure of the specimen after 2 cycles where a cycle includes loading and reverse loading. For the second load case with constant maximum loads $\Delta u_{\text{ref}}^{\text{max}} = 0.28\,\text{mm}$ and $\Delta u_{\text{ref}}^{\text{min}} = -0.25\,\text{mm}$ are measured which leads to failure after 6.5 cycles under compressive loading. A different approach was used for the experiments shown in Fig. 2(c, d): here the maximum and the minimum relative displacement have been increased in every cycle. For instance in (c) the displacement increase $\Delta u_{\text{ref}}^{\text{inc}} = 0.15\,\text{mm}$ has been applied leading to fracture after 3 cycles at $\Delta u_{\text{ref}}^{\text{max}} = 0.58\,\text{mm}$. For the load case shown in (d) $\Delta u_{\text{ref}}^{\text{inc}} = 0.05\,\text{mm}$ has been used and $\Delta u_{\text{ref}}^{\text{max}} = 0.48\,\text{mm}$ was reached whereby the test specimen failed under compressive loading. At this point, it is emphasized that the load cases shown in Fig. 2(a, c) failed under tension and that the load cases in Fig. 2(b, d) failed under compression. The corresponding numerically calculated load-displacement curves over all reflect nicely the experimentally obtained ones whereas under constant maximum loads the minimum force is slightly overestimated whereas for the load cases with load increase the maximum load is slightly underestimated.

The strains on the specimen surfaces have been evaluated by digital image correlation (DIC) and by matching the relative displacements Δu_{ref} of the numerical simulations the corresponding simulation results can be assigned. Fig. 3 displays the experimentally and numerically obtained first principal strain $\mathbf{A}_1$ shortly before fracture. The results are displayed for the region marked by a red box in Fig. 1(a) and a suitable scale was selected for each load case. Overall, good agreement between experimental (EXP) and numerical (SIM) results can be recognized. The experiments that failed under tension loading (a,c) indicate a slightly to the left inclined shear band with maximum values of (a) 0.25 and (c) 0.35 which results from the more elevated relative displacement at the end of experiment (c), see Fig. 2(a, c). The experiment with 6.5 cycles and constant maximum loading (b) fractured under compressive loading and indicates a sharp band of elevated strains with values up to 0.13 and is inclined to the right. The experimental data (b, left) is more noisy and consequently the sharp characteristic is less visible. The experiment with 8.5 cycles and load increase indicates a to the left inclined band with elevated strains. Unlike in (b), the maximum values (0.17) are not continuous across the height but are 'flame-shaped' towards the center. The experimental data is not as well resolved here either. Thus, the influences of the load history is clearly visible, which is additionally emphasized by slightly increased strains outside the band. Consequently, the loading direction as well as the loading history influences the inclination and occurrence of the shear band.

The accumulated principal damage strains $\mathbf{A}_{(i)}^{\text{da}}$ based on Eq. (4) are accessible through the numerical simulations. Fig. 4 shows the calculated first principal damage strain $\mathbf{A}_1^{\text{da}}$ for all four load cases shortly before fracture on the left

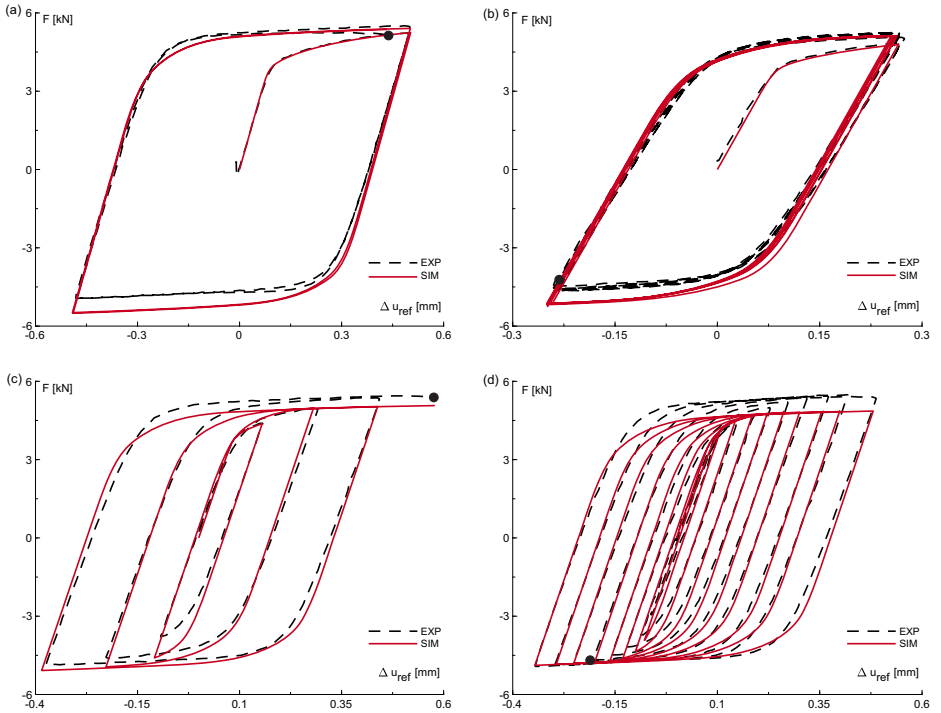

Fig. 2: Load-displacement curves: (a) 2 cycles constant maximum load; (b) 6.5 cycles constant maximum load; (c) 3 cycles with load increase and (d) 8.5 cycles with load increase.

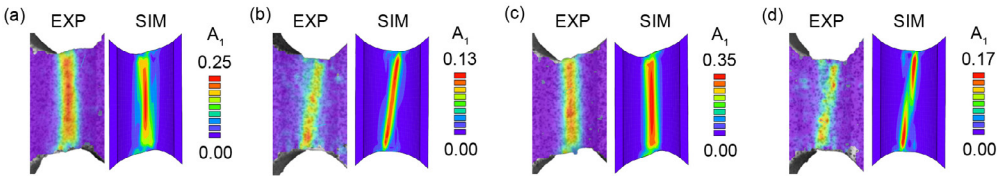

Fig. 3: First principal strain before fracture, left experimentally obtained and right numerically calculated: (a) 2 cycles constant maximum load; (b) 6.5 cycles constant maximum load; (c) 3 cycles with load increase and (d) 8.5 cycles with load increase.

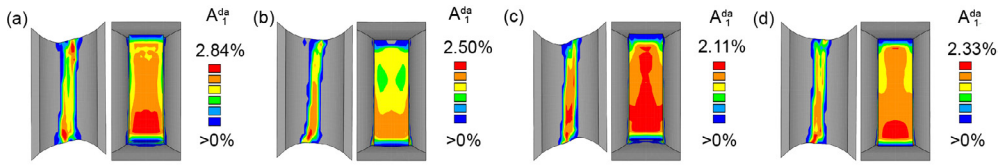

Fig. 4: Numerically calculated first principal damage strain before fracture: (a) 2 cycles constant maximum load; (b) 6.5 cycles constant maximum load; (c) 3 cycles with load increase and (d) 8.5 cycles with load increase.

side similar to Fig. 3 on the surface of the notched area and on the right side of the cross section in the center of the notch. For 2 cycles with constant maximum load $\mathbf{A}_1^{da}$ indicates an almost symmetrical distribution to the notch center (a, left) and based on the load case highest values up to 2.84%. With a larger number of cycles, the symmetry is lost (b-d) and concentrations of the first principal damage strain tend to occur in the lower half of the notch. Furthermore, the formation of a sharp band as observed for the first principal strains $\mathbf{A}_1$ in Fig. 3 can not be recognized.

Finally the ductile damage process leads to fracture of the specimens in the notched cross-section whereby in most cases, both notches fracture at the same time. Fig. 5 shows a cutout (see red box in Fig. 1(a)) from a photo of the

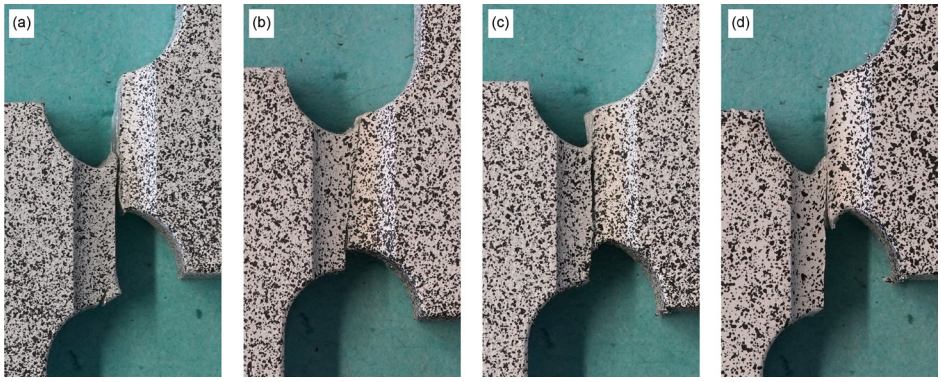

Fig. 5: Fractured specimens: (a) 2 cycles constant maximum load; (b) 6.5 cycles constant maximum load; (c) 3 cycles with load increase and (d) 8.5 cycles with load increase.

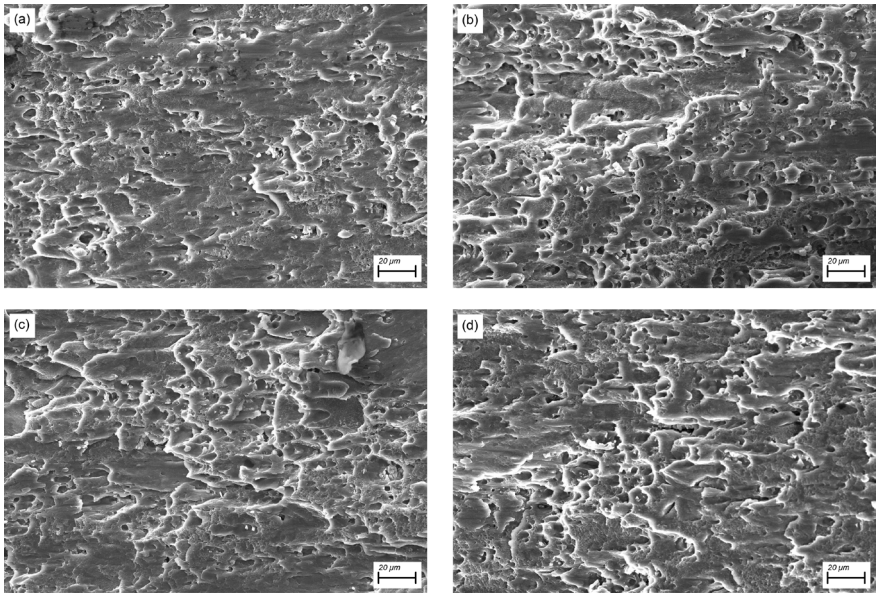

Fig. 6: SEM images of fracture surface: (a) 2 cycles constant maximum load; (b) 6.5 cycles constant maximum load; (c) 3 cycles with load increase and (d) 8.5 cycles with load increase.

reassembled fractured specimens for all 4 experiments. The fracture lines follow directly from the strain distributions displayed in Fig. 3. The experiments that fractured under tension loading indicate a fracture line that is parallel to the notch with slight inclination to the left (a, c) and the ones that fractured under compression have a fracture line that is inclined to the right. Unfortunately, after fracture there might be significant contact between the fracture surfaces which might have an influence on surface texture. The corresponding numerical simulations indicated a stress triaxiality, defined as the ratio of the mean and the von Mises equivalent stress, between 0.12 (tension) and -0.14 (compressive loading) which means values very close to zero which corresponds to a shear loading state. The SEM images of the fracture surfaces displayed in Fig. 6 for all four load cases indicate clearly fracture caused by ductile damage in the shear range characterized by micro shear cracks with a very small amount of voids, see Brünig et al. (2011). All four load cases indicate a comparable texture reflecting the stress state and a similar damage evolution (see Fig. 4) and the loading history has in this case a rather minor influence on the appearance of the fracture surface.

5. Conclusions

This publication summarizes the continuum damage model for the description of elastic-plastic, ductile damaged material behavior for non-proportional and cyclic loads. A new series of tests has been performed on a standard testing machine with cyclic loading including reverse loading and focus on shear failure. Both, cycles with constant amplitude and cycles with increasing amplitude were applied and the corresponding results are evaluated and discussed. The results clearly show that a target-oriented investigation of the ductile damage behavior under cyclic load with stresses in the shear range is possible with the applied specimen on a standard testing machine. The accompanying numerical simulations clearly show that the propagation of the damage varies significantly depending on the load case. The SEM images of the fracture surfaces, on the other hand, confirm that the development of damage and the subsequent crack occurred under similar stress conditions with a stress triaxiality of around zero. In the future focus should be given on the expansion of the experimental series. Specially loading scenarios with more extensive compressive than tension loads or with more extensive tension then compressive loads are of interest. This can help to obtain indications of a possible reduction in damage under cyclic load. A slight inclination of the notches also makes it possible to realize load changes between triaxialities that deviate slightly from zero. However, tests with biaxially loaded specimens are necessary to cover an even wider range of stress triaxialities.

Acknowledgements

The project has been funded by the Deutsche Forschungsgemeinschaft (DFG, German Research Foundation) – project number 322157331, this financial support is gratefully acknowledged. The SEM images of the fracture surfaces presented in this paper were performed at the Institut für Werkstoffe im Bauwesen, Universität der Bundeswehr München, and the support of Wolfgang Saur is gratefully acknowledged.

References

Algarni, M., Bai, Y., Zwawi, M., Ghazali, S., 2019. Damage evolution due to extremely low-cycle fatigue for inconel 718 alloy. Metals 9, 1109. doi:10.3390/met9101109.

Brünig, M., Albrecht, D., Gerke, S., 2011. Modeling of ductile damage and fracture behavior based on different micromechanisms. International Journal of Damage Mechanics 20, 558–577. doi:10.1177/1056789510386860.

Brünig, M., Chyra, O., Albrecht, D., Driemeier, L., Alves, M., 2008. A ductile damage criterion at various stress triaxialities. International Journal of Plasticity 24, 1731–1755. doi:10.1016/j.ijplas.2007.12.001.

Cao, J., Lee, W., Cheng, H.S., Seniw, M., Wang, H.P., Chung, K., 2009. Experimental and numerical investigation of combined isotropic-kinematic hardening behavior of sheet metals. International Journal of Plasticity 25, 942–972. doi:10.1016/j.ijplas.2008.04.007.

Daroju, S., Kuwabara, T., Knezevic, M., 2022. Experimental characterization and crystal plasticity modeling of dual-phase steels subjected to strain path reversals. Mechanics of Materials 168, 104293. doi:10.1016/j.mechmat.2022.104293.

Kanvinde, A.M., Deierlein, G.G., 2007. Cyclic void growth model to assess ductile fracture initiation in structural steels due to ultra low cycle fatigue. Journal of Engineering Mechanics 133, 701–712. doi:10.1061/(ASCE)0733-9399(2007)133:6(701).

Klingbeil, D., Svendsen, B., Reusch, F., 2016. Gurson-based modelling of ductile damage and failure during cyclic loading processes at large deformation. Engineering Fracture Mechanics 160, 95–123. doi:10.1016/j.engfracmech.2016.03.023.

Marcadet, S.J., Mohr, D., 2015. Effect of compression–tension loading reversal on the strain to fracture of dual phase steel sheets. International Journal of Plasticity 72, 21–43. doi:10.1016/j.ijplas.2015.05.002.

Murakami, Y., Miller, K., 2005. What is fatigue damage? A view point from the observation of low cycle fatigue process. International Journal of Fatigue 27, 991–1005. doi:10.1016/j.ijfatigue.2004.10.009.

Shi, Y., Wang, M., Wang, Y., 2011. Experimental and constitutive model study of structural steel under cyclic loading. Journal of Constructional Steel Research 67, 1185–1197. doi:10.1016/j.jcsr.2011.02.011.

Voyiadjis, G.Z., Hoseini, S.H., Farrahi, G.H., 2013. A plasticity model for metals with dependency on all the stress invariants. Journal of Engineering Materials and Technology 135, 011002. doi:10.1115/1.4007386.

Wei, Z., Gerke, S., Brünig, M., 2023. Damage and fracture behavior under non-proportional biaxial reverse loading in ductile metals: Experiments and material modeling. International Journal of Plasticity 171, 103774. doi:10.1016/j.ijplas.2023.103774.

Wei, Z., Gerke, S., Brünig, M., 2024. Numerical analysis of non-proportional biaxial reverse experiments with a two-surface anisotropic cyclic plasticity-damage approach. Computer Methods in Applied Mechanics and Engineering 419, 116630. doi:10.1016/j.cma.2023.116630.

Wei, Z., Zistl, M., Gerke, S., Brünig, M., 2022. Analysis of ductile damage and fracture under reverse loading. International Journal of Mechanical Sciences 228, 107476. doi:10.1016/j.ijmecsci.2022.107476.

Wu, H., Zhang, C., Yang, H., Zhuang, X., Zhao, Z., 2024. Extended Gurson-Tvergaard-Needleman model considering damage behaviors under reverse loading. International Journal of Mechanical Sciences 272, 109196. doi:10.1016/j.ijmecsci.2024.109196.